Aging and Disease
www.aginganddisease.org
Early access date: August 9, 2026
http://dx.doi.org/10.14336/AD.2026.0432

Original Article

KDM4C inhibition reinforces NK cell cytotoxicity through the cGAS–STING pathway in *TP53*-mutated AML

Xinyi Zhang[1,2,3], Huilan Liu[1,2,4*], Liangquan Geng[1], Panpan Huang[5], Mengqing Gao[1,2], Qian Fan[1,2], Kaishuang Jiang[1,2], Na Zhao[1,2], Xuxu Zhao[2,6], Huaiping Zhu[5], Cihangir Duy[7,8,9], Haiming Wei[1,2*], Dongyao Wang[1,2,3,6*]

[1]Department of Hematology, The First Affiliated Hospital of USTC; National Key Laboratory of Immune Response and Immunotherapy, Division of Life Sciences and Medicine, University of Science and Technology of China; Institute of Immunology, University of Science and Technology of China, Hefei, Anhui, 230027, China. [2]Blood and Cell Therapy Institute, Anhui Provincial Key Laboratory of Blood Research and Applications, University of Science and Technology of China, Hefei, Anhui, 230027, China. [3]Cell and Regenerative Medicine Research and Development Center, Zhongke Hefei Institute of Technology Innovation Engineering, Hefei, Anhui, 230088, China. [4]Department of Transfusion, The First Affiliated Hospital of USTC, Division of Life Sciences and Medicine, University of Science and Technology of China, Hefei, Anhui, 230027, China. [5]Department of Laboratory Medicine, The First Affiliated Hospital of USTC, Division of Life Sciences and Medicine, University of Science and Technology of China, Hefei, Anhui, 230027, China. [6]Anhui Provincial Key Laboratory of Tumor Evolution and Intelligent Diagnosis and Treatment, Bengbu, Anhui, 233030, China. [7]Nuclear Dynamics and Cancer Program, Fox Chase Cancer Center, Philadelphia, Pennsylvania. PA 19111, USA. [8]Cancer Epigenetics Institute, Fox Chase Cancer Center, Philadelphia, Pennsylvania. PA 19111, USA. [9]Weill Cornell Medicine, New York, NY 10021, USA

[Received April 9, 2026; Revised August 4, 2026; Accepted August 7, 2026]

ABSTRACT: *TP53*-mutated acute myeloid leukemia (AML) is associated with an extremely poor prognosis and is refractory to conventional chemotherapy and allogeneic hematopoietic stem cell transplantation (allo-HSCT). We identified high expression of lysine demethylase 4C (KDM4C) in AML, particularly in *TP53*-mutated AML. Pharmacological inhibition of KDM4C with QC6352 predominantly induced apoptosis in *TP53*-wild-type AML cells, whereas it caused limited apoptosis but pronounced senescence and growth arrest in *TP53*-mutated AML cells. In *TP53*-mutated AML cells, QC6352 induced senescence-associated cytosolic DNA accumulation and activated the cyclic GMP-AMP synthase (cGAS)–stimulator of interferon genes (STING) pathway, leading to the upregulation of NK cell-activating ligands and enhancing NK cell-mediated cytotoxicity. *In vivo*, QC6352 effectively attenuated AML progression, and its combination with NK cell therapy further reduced leukemic burden and prolonged survival in mice. Collectively, these findings demonstrate that pharmacological KDM4C inhibition with QC6352 induces cellular senescence and enhances the intrinsic immunogenicity of *TP53*-mutated AML cells through activation of the cGAS–STING pathway. The study supports KDM4C inhibition as a potential therapeutic strategy for *TP53*-mutated AML, particularly in patients receiving NK cell-based immunotherapy or undergoing allo-HSCT.

Keywords: NK cells, AML, KDM4C, senescence, immunotherapy

***Correspondence should be addressed to:** Dr. Huilan Liu (Email: huilanl@ustc.edu.cn), Dr. Haiming Wei (Email: ustcwhm@ustc.edu.cn), and Dr. Dongyao Wang (Email: dywsn@ustc.edu.cn). University of Science and Technology of China, 443 Huangshan Road, Hefei, Anhui, 230027, China.

INTRODUCTION

Tumor protein p53 (*TP53*) is one of the most frequently mutated genes in cancer [1]. Acute myeloid leukemia (AML) is a heterogeneous hematologic malignancy characterized by the clonal expansion of immature myeloid cells in the bone marrow [2]. The overall prognosis of patients with AML remains poor, particularly among those with *TP53*-mutated or *TP53*-deleted disease [3]. *TP53* mutations occur in approximately 5-10% of AML cases and are associated with an extremely poor prognosis [4]. Patients with *TP53*-mutated AML frequently exhibit resistance to conventional chemotherapy and have a high risk of relapse after allogeneic hematopoietic stem cell transplantation (allo-HSCT) [5, 6]. *TP53* is a key regulator of apoptosis, cell-cycle arrest and cellular responses to stress. Beyond its role in cell-intrinsic tumor suppression, *TP53* also participates in the regulation of antitumor immunity. Studies across several tumor types have shown that *TP53* abnormalities may impair type I interferon signaling and antigen presentation, enhance immune-checkpoint signaling, and promote the production of immunosuppressive factors [7]. Collectively, these alterations may reduce the recognition and elimination of malignant cells by both innate and adaptive immune cells.

Natural killer (NK) cells are major effectors of innate antitumor immunity and are particularly important for the control of hematologic malignancies. They mediate direct cytotoxicity against malignant or stressed cells without prior antigen sensitization. NK cells participate in the surveillance and elimination of residual tumor cells after chemotherapy or radiotherapy and contribute to the graft-versus-leukemia (GVL) effect following allo-HSCT [8, 9]. NK-cell activity is determined by the balance between activating and inhibitory signals received from target cells. However, AML cells can disrupt this balance through several mechanisms. They may reduce the surface expression of activating ligands, including the NKG2D ligands MICA/B and members of the ULBP family [8], or release soluble forms of these ligands that impair NKG2D signaling. AML cells may also suppress endogenous type I interferon (IFN-I) production, thereby attenuating NK-cell priming and antileukemic responses [10]. These mechanisms weaken both endogenous NK-cell surveillance and the efficacy of adoptive NK-cell therapy.

Cellular senescence may provide a mechanism for both restricting tumor growth and enhancing immune recognition. Therapy-induced senescence induces sustained growth arrest and is often accompanied by oxidative stress, persistent DNA damage, and cytosolic DNA accumulation in tumor cells. These changes can activate the cyclic GMP–AMP synthase (cGAS)–stimulator of interferon genes (STING) pathway [11, 12]. Upon sensing cytosolic DNA, cGAS produces cyclic GMP–AMP (cGAMP), which activates STING and subsequently promotes the production of type I interferons, pro-inflammatory cytokines, and chemokines [13, 14]. In tumor cells, activation of the cGAS–STING pathway can increase the expression of stress-induced immune ligands, including NKG2D ligands, thereby enhancing NK-cell recognition and cytotoxicity [15]. Thus, senescence-associated cGAS–STING activation may link tumor-cell growth arrest to NK cell-mediated immune clearance.

Epigenetic dysregulation is a hallmark of AML and contributes to leukemic transformation, treatment resistance, and immune escape. Recurrent abnormalities in epigenetic regulation are also commonly observed across hematologic malignancies, including leukemia and lymphoma [16]. Histone lysine-specific demethylase 4C (KDM4C), a key enzyme in epigenetic modification, catalyzes the demethylation of the histone marks H3K9me3 and H3K36me3 [17], thereby modulating downstream gene expression and contributing to tumorigenesis and antitumor immunity [18, 19]. KDM4C inhibition has been shown to suppress tumor growth in basal-like breast cancer and enhance $CD8^+$ T-cell-mediated antitumor immunity in lung cancer [20]. However, the role of KDM4C in AML progression and the effects of KDM4C targeting on NK-cell-mediated antileukemic immunity remain largely unknown.

A previous study showed that genetic depletion of KDM4C suppressed AML growth and prolonged survival in murine models. However, the expression profile of KDM4C in human AML samples, its association with clinical outcomes, and its broader biological roles in AML remain incompletely understood. In particular, whether KDM4C regulates antileukemic immunity has not been explored. In this study, we investigated the expression and clinical significance of KDM4C in AML and further examined the effects of pharmacological KDM4C inhibition on AML progression and NK-cell-mediated antileukemic responses.

MATERIALS AND METHODS

Human samples

Primary AML cells and normal bone marrow mononuclear cells (BMMCs) were isolated from residual bone marrow aspirates remaining after routine diagnostic testing from patients with AML (n = 22) and healthy donors (n = 10). NK cells used in the *in vitro* assays were purified from the bone marrow of healthy donors. All human samples were collected in accordance with a

protocol approved by the Ethics Committee of the First Affiliated Hospital of the University of Science and Technology of China (2023-N(H)-254; Hefei, China). Written informed consent was obtained from all patients. The clinical characteristics of patients are shown in Supplementary Table 1. The identities and experimental use of individual primary AML samples are provided in Supplementary Table 2.

Mice

Female NOD/ShiLtJGpt-Prkdc^{em26Cd52}IL-2rg^{em26Cd22}/Gpt (NCG) mice were purchased from GemPharmatech. All mice were kept in specific pathogen-free conditions. All animal experiments were performed in accordance with the National Guidelines for Animal Usage in Research (China) and were approved by the Ethics Committee of the Institute of Health and Medicine, Hefei Comprehensive National Science Center (IHM-AP-2025-007).

Human AML xenograft models and treatments

In the first set of experiments, 6-week-old female NCG mice were injected with 1×10^6 THP-1 cells via the tail vein to establish a human AML xenograft model. The mice were randomly assigned to four groups (n = 12 mice per group). Group 1 received PBS as the control; group 2 received QC6352 (MedChemExpress, Cat. # HY-104048); group 3 received 5×10^6 NK cells; and group 4 received 5×10^6 NK cells plus QC6352. Treatment was initiated on Day 7 after THP-1 cell injection. QC6352 was administered intraperitoneally (i.p.) at 10 mg/kg every other day (Qod). Human NK cells were administered via the tail vein on Day 7. To support the *in vivo* survival of the adoptively transferred NK cells, mice receiving NK-cell infusion were administered 50,000 U of IL-2 (Jiangsu Kingsley Pharmaceuticals) intraperitoneally every 2 days. On Day 14, six mice from each group were randomly euthanized, and bone marrow samples from the NK-cell and NK-cell-plus-QC6352 groups were collected for flow cytometric evaluation of the phenotype and function of the adoptively transferred human NK cells. On Day 30, bone marrow samples were collected from the remaining six mice in each group to assess THP-1 cell engraftment by flow cytometry.

In the second set of experiments, 6-week-old female NCG mice were injected via the tail vein with 1×10^5 luciferase-expressing U937 (U937-Luc) cells to establish a human AML xenograft model. Leukemic engraftment was confirmed by bioluminescence imaging (BLI) on Day 6 after U937-Luc cell injection, after which the mice were randomly assigned to six groups (n = 7 mice per group). Treatment was initiated immediately after confirmation of leukemic engraftment. Group 1 received PBS as the control; group 2 received QC6352 (10 mg/kg, Qod, i.p.); group 3 received 5×10^5 NK cells; group 4 received 5×10^5 NK cells plus QC6352; group 5 received 5×10^5 NK cells plus QC6352 plus H-151 (Selleck, Cat. # S6652; 15 mg/kg, Qod, i.p.); and group 6 received 5×10^5 NK cells plus di-ABZI (Selleck, Cat. # S8796; 3 mg/kg, Qod, i.p.). To support *in vivo* survival of NK cells, mice receiving NK-cell infusion were administered 50,000 U IL-2 intraperitoneally every 2 days. Leukemia burden was monitored by BLI using the IVIS Spectrum Imaging System (PerkinElmer) at the indicated time points. Quantitative imaging data were analyzed using Living Image software (PerkinElmer).

In the third set of experiments, 6-week-old female NCG mice were injected via the tail vein with 1×10^5 U937-Luc cells to establish a human AML xenograft model. Leukemic engraftment was confirmed by bioluminescence imaging (BLI) on Day 9 after U937-Luc cell injection, after which the mice were randomly assigned to four groups (n = 8 mice per group). Treatment was initiated immediately after confirmation of leukemic engraftment. Group 1 received PBS as the control; group 2 received QC6352 (10 mg/kg, Qod, i.p.); group 3 received 1×10^6 peripheral blood mononuclear cells (PBMCs); and group 4 received 1×10^6 PBMCs plus QC6352. To support *in vivo* survival of PBMCs, mice receiving PBMC infusion were administered 50,000 U IL-2 intraperitoneally every 2 days. Leukemia burden was monitored by BLI using the IVIS Spectrum Imaging System at the indicated time points. Quantitative imaging data were analyzed using Living Image software.

In the fourth set of experiments, 6-week-old female NCG mice were injected with 1×10^6 THP-1 cells via the tail vein to establish a human AML xenograft model. The mice were randomly assigned to five groups (n = 6 mice per group). Group 1 received PBS as the control; group 2 received QC6352 (10 mg/kg, Qod, i.p.); group 3 received 1×10^7 PBMCs; group 4 received 1×10^7 PBMCs plus QC6352; and group 5 received 1×10^7 NK-cell-depleted PBMCs plus QC6352. For group 5, NK cells were depleted from the PBMCs using anti-CD56 magnetic beads before adoptive transfer. Treatment was initiated on Day 7 after THP-1 cell injection. To support *in vivo* survival of PBMCs, mice receiving PBMC infusion were administered 50,000 U IL-2 intraperitoneally every 2 days. Bone marrow samples were collected on Day 30, and THP-1 cell engraftment in the bone marrow was assessed by flow cytometry.

Human NK-cell isolation and culture

NK cells used in the *in vitro* co-culture and cytotoxicity assays and *in vivo* adoptive-transfer experiments were

isolated from bone marrow mononuclear cells (BMMCs) obtained from healthy donors using a magnetic-activated cell sorting (MACS) kit (Miltenyi Biotec, Cat. # 130-092-657). The purity of the NK cells was > 90% in all experiments. The isolated NK cells were cultured in RPMI 1640 medium (VivaCell, Cat. # C3010-0500) supplemented with 10% fetal bovine serum (FBS; Sigma, Cat. # F7524) and 1% penicillin–streptomycin (Gibco, Cat. # 15140122). NK cells were first stimulated for 24 h with 200 U/mL IL-2 (PeproTech, Cat. # 210-12).

Flow cytometry experiments

Single-cell suspensions were stained with fluorochrome-conjugated antibodies against human cell-surface or intracellular antigens. Before antibody staining, cells were incubated with human Fc-blocking reagent (BD Biosciences, Cat. # 564220) to minimize nonspecific antibody binding to Fc receptors. Matched isotype controls were included where appropriate. For intracellular staining, cells were fixed and permeabilized using the Foxp3/Transcription Factor Staining Buffer Set (Invitrogen, Cat. #00-5523-00) according to the manufacturer's instructions. For indirect immuno-fluorescence staining using fluorescently conjugated secondary antibodies, secondary-antibody-only controls were included to assess nonspecific binding of the secondary antibody. Data were collected using the BD LSR II flow cytometer (BD Biosciences, USA) and analyzed with FlowJo software (Tree Star, USA).

The following antibodies and reagents were used for flow cytometry: APC-Cy7 mouse anti-human CD3 (BD Biosciences, Cat. #557832); BV605 mouse anti-human CD3 (BioLegend, Cat. # 344836); PerCP-Cy5.5 mouse anti-human CD3 (BD Biosciences, Cat. #552852); BV421 mouse anti-human CD56 (BioLegend, Cat. #362552); PE-Cy7 mouse anti-human CD56 (BD Biosciences, Cat. # 557747); PerCP-Cy5.5 mouse anti-human CD8 (BioLegend, Cat. #344710); FITC mouse anti-human CD8 (BD Biosciences, Cat. #570893); BV650 mouse anti-human CD4 (BioLegend, Cat. #317436); APC-Cy7 mouse anti-human CD45 (BD Biosciences, Cat. #557833); BV510 mouse anti-human CD45 (BD Biosciences, Cat. #563204); FITC mouse anti-human CD33 (BD Biosciences, Cat. #555626); BV605 mouse anti-human CD33 (BD Biosciences, Cat. #740400); PE mouse anti-human CD34 (BD Biosciences, Cat. #550619); PerCP-Cy5.5 mouse anti-human CD38 (BioLegend, Cat. #303522); PE-Cy7 mouse anti-human CD69 (BioLegend, Cat. #310912); APC mouse anti-human CD25 (BioLegend, Cat. #356110); APC mouse anti-human MICA/B (BioLegend, Cat. #320908); PE-Cy7 mouse anti-human MICA/B (Invitrogen, Cat. #MA5-38728); PerCP mouse anti-human ULBP1 (R&D Systems, Cat. #FAB1380C); PE mouse anti-human ULBP3 (R&D Systems, Cat. #FAB1517P); APC mouse anti-human ULBP2/5/6 (R&D Systems, Cat. #FAB1298R); Alexa Fluor 647 rabbit monoclonal anti-calreticulin (Abcam, Cat. #ab196159); APC-Cy7 mouse anti-human CD11b (BD Biosciences, Cat. #557754); APC-Cy7 mouse anti-human CD14 (BD Biosciences, Cat. #557831); PE-Cy7 mouse anti-human CD15 (BioLegend, Cat. #301924); PE-Cy7 mouse anti-human NKG2D (BioLegend, Cat. #320812); APC mouse anti-human NKp30 (BioLegend, Cat. #325210); FITC mouse anti-human DNAM-1/CD226 (BD Biosciences, Cat. #559788); FITC anti-human NKG2A/CD159a (Miltenyi Biotec, Cat. #130-113-565); Alexa Fluor 647 mouse anti-human Ki-67 (BD Biosciences, Cat. #571537); APC mouse anti-human CD107a (BD Biosciences, Cat. #560 664); FITC mouse anti-human IFN-γ (BD Biosciences, Cat. #554700); PE mouse anti-human TNF (BD Biosciences, Cat. # 559321); BV421 mouse anti-human granzyme B (BD Biosciences, Cat. #563389); BV510 mouse anti-human granzyme B (BD Biosciences, Cat. #563388); rabbit polyclonal anti-KDM4C/ JMJD2C (Invitrogen, Cat. #PA5-23065); rabbit monoclonal anti-γH2AX (phospho-Ser139; Abcam, Cat. #ab81299); Alexa Fluor 488 goat anti-rabbit IgG (H+L) secondary antibody (Abcam, Cat. #ab150077); FITC Annexin V (BD Biosciences, Cat. #556420); PE Annexin V (BD Biosciences, Cat. #556421); 7-AAD (BD Biosciences, Cat. #559925); Alexa Fluor 647 rabbit anti-active caspase-3 (BD Biosciences, Cat. #570408); FITC mouse IgG1, κ (BD Biosciences, Cat. #555748); PE mouse IgG1, κ (BD Biosciences, Cat. # 555749); PerCP-Cy5.5 mouse IgG1, κ (BD Biosciences, Cat. # 552834); PerCP mouse IgG1, κ (BD Biosciences, Cat. #559425); BV421 mouse IgG1, κ (BD Biosciences, Cat. #569394); BV510 mouse IgG1, κ (BD Biosciences, Cat. #562946); APC mouse IgG1, κ (BD Biosciences, Cat. #550854); APC-Cy7 mouse IgG1, κ (BD Biosciences, Cat. #557873); and PE-Cy7 mouse IgG1, κ (BD Biosciences, Cat. #557872).

NK-cell-mediated killing assays and co-culture

THP-1 and U937 cells and primary AML blasts were used as target cells. Target cells were pretreated with the indicated drugs for 48 h, whereas control cells were treated with vehicle alone. After treatment, the cells were collected by centrifugation and washed thoroughly to remove residual drugs. For NK-cell-mediated cytotoxicity assays, target cells were labeled with the CellTrace Violet Cell Proliferation Kit (Invitrogen, Cat. #C34557) and then co-cultured with NK cells at the indicated effector-to-target (E: T) ratios in 96-well plates for 4 h. Target-cell apoptosis was assessed by flow cytometry after staining with 7-AAD and Annexin V. To assess NK-cell

degranulation and intracellular cytokine production, pretreated target cells were co-cultured with NK cells at an E: T ratio of 5:1 for 6 h. The expression of CD107a, IFN-γ, TNF-α, and granzyme B in NK cells was subsequently analyzed by flow cytometry. To evaluate NK-cell activation and receptor expression, pretreated target cells were co-cultured with NK cells at an E: T ratio of 5:1. Surface expression of CD69 was analyzed after 24 h of co-culture, whereas the expression of NKG2D, NKp30, and DNAM-1 was analyzed after 48 h by flow cytometry.

RNA-sequencing

Total RNA was extracted from 1×10^6 THP-1 and U937 cells cultured in complete RPMI 1640 medium with or without 30 nM QC6352 for 48 h using TRIzol Reagent (Invitrogen, Cat. #15596018), according to the manufacturer's instructions. RNA-sequencing libraries were prepared from the samples (n = 3 per group) and sequenced on an Illumina NovaSeq X Plus platform (Illumina, San Diego, CA, USA). All samples were processed in a single batch, including RNA extraction, library preparation, and sequencing, under identical conditions. Therefore, no additional batch correction was performed. Gene expression levels were quantified as transcripts per million (TPM) for visualization purposes. Differential expression analysis was performed using DESeq2 based on raw gene-level count data. Genes with a false discovery rate (FDR) of < 0.05 and an absolute fold change of ≥ 2 were considered differentially expressed genes (DEGs). Gene Ontology (GO) enrichment analysis of DEGs was performed using the OmicSmart platform. Gene Set Enrichment Analysis (GSEA) was performed using the GSEA software with gene sets obtained from the Molecular Signatures Database (MSigDB). The raw sequencing data generated in this study have been deposited in the Genome Sequence Archive for Human (GSA-Human) of the National Genomics Data Center, China National Center for Bioinformation/Beijing Institute of Genomics, Chinese Academy of Sciences, under accession number HRA013401, and are publicly accessible at https://ngdc.cncb.ac.cn/gsa-human.

Statistical analysis

For *in vitro* cell experiments using cell lines, n represents the number of independent biological replicates performed using separately prepared cell cultures. For experiments using primary AML samples, n represents the number of independent patients. Technical replicates within each biological replicate were averaged to generate a single value for statistical analysis. Unless otherwise indicated, quantitative *in vitro* experiments included six independent biological replicates.

Normality was assessed using the Shapiro-Wilk test. Data that did not significantly deviate from a normal distribution were analyzed using a two-tailed paired or unpaired Student's *t* test, one-way analysis of variance (ANOVA), or repeated-measures ANOVA, as appropriate. Tukey's multiple comparisons test was used following ANOVA when multiple-group comparisons were performed. When the assumption of normality was not met, the Wilcoxon matched-pairs signed-rank test, Mann–Whitney U test, Kruskal–Wallis test, or Friedman test was used, as appropriate. Dunn's multiple comparisons test was performed following the Kruskal–Wallis or Friedman test. All statistical analyses were performed using GraphPad Prism 10. The statistical tests and sample sizes used for individual experiments are specified in the corresponding figure legends. Unless otherwise indicated, data are presented as the mean ± standard deviation (SD). Statistical significance was defined as follows: $*P < 0.05$; $**P < 0.01$; $***P < 0.001$; $****P < 0.0001$.

RESULTS

KDM4C inhibition suppressed the proliferation of *TP53*-mutated AML cells.

We first evaluated *KDM4C* mRNA expression in AML using the GEPIA database. *KDM4C* expression was significantly higher in AML samples than in normal bone marrow samples (Fig. 1A). Among various types of cancers, AML exhibited the highest *KDM4C* mRNA expression (Supplementary Fig. 1A), suggesting a potentially prominent role for KDM4C in AML. Kaplan–Meier survival analysis further showed that high *KDM4C* expression was associated with shorter overall survival in patients with AML (Fig. 1B). Immunohistochemical analysis demonstrated higher KDM4C protein expression in bone marrow samples from patients with AML than in non-AML controls (Fig. 1C). At the patient level, the proportion of $KDM4C^+$ cells was significantly higher in *TP53*-mutated AML than in non-AML controls. Flow cytometric analysis further confirmed elevated KDM4C expression in AML blasts, with a similar tendency toward higher expression in *TP53*-mutated samples (Fig. 1D and E).

Patients with *TP53*-mutated AML have shorter median overall survival and lower response rates to induction chemotherapy and venetoclax-based therapies than patients with *TP53*-wild-type AML [21]. Previous studies have shown that KDM4C inhibition can induce senescence in gastric cancer cells harboring *TP53* mutations [22]. We therefore examined *TP53*-wild-type

and *TP53*-mutated AML cell lines, all of which expressed KDM4C protein (Supplementary Fig. 1B). KDM4C protein expression was higher in *TP53*-mutated AML cell lines, including THP-1, U937, KG-1a, and Kasumi-1, than in the *TP53*-wild-type AML cell lines MOLM-13 and OCI-AML3 (Supplementary Fig. 1B). To investigate the effects of targeting KDM4C in AML cells, we used the small-molecule inhibitor QC6352 for pharmacological inhibition. QC6352 exhibits an IC_{50} of 35 nM against KDM4C and shows greater biochemical potency against KDM4C than against the other histone demethylases tested [17]. QC6352 treatment significantly inhibited the growth of both *TP53*-wild-type and *TP53*-mutated AML cells *in vitro* (Fig. 1F and Supplementary Fig. 1C). In *TP53*-wild-type cells, QC6352 treatment induced a marked increase in apoptosis (Supplementary Fig. 1D). In contrast, QC6352 induced substantially less apoptosis in *TP53*-mutated cells than in *TP53*-wild-type cells (Fig. 1G). Analysis of active caspase-3 further supported this difference (Supplementary Fig. 2). Together, these findings indicate that QC6352 suppresses the growth of *TP53*-mutated AML cells predominantly through an apoptosis-independent mechanism.

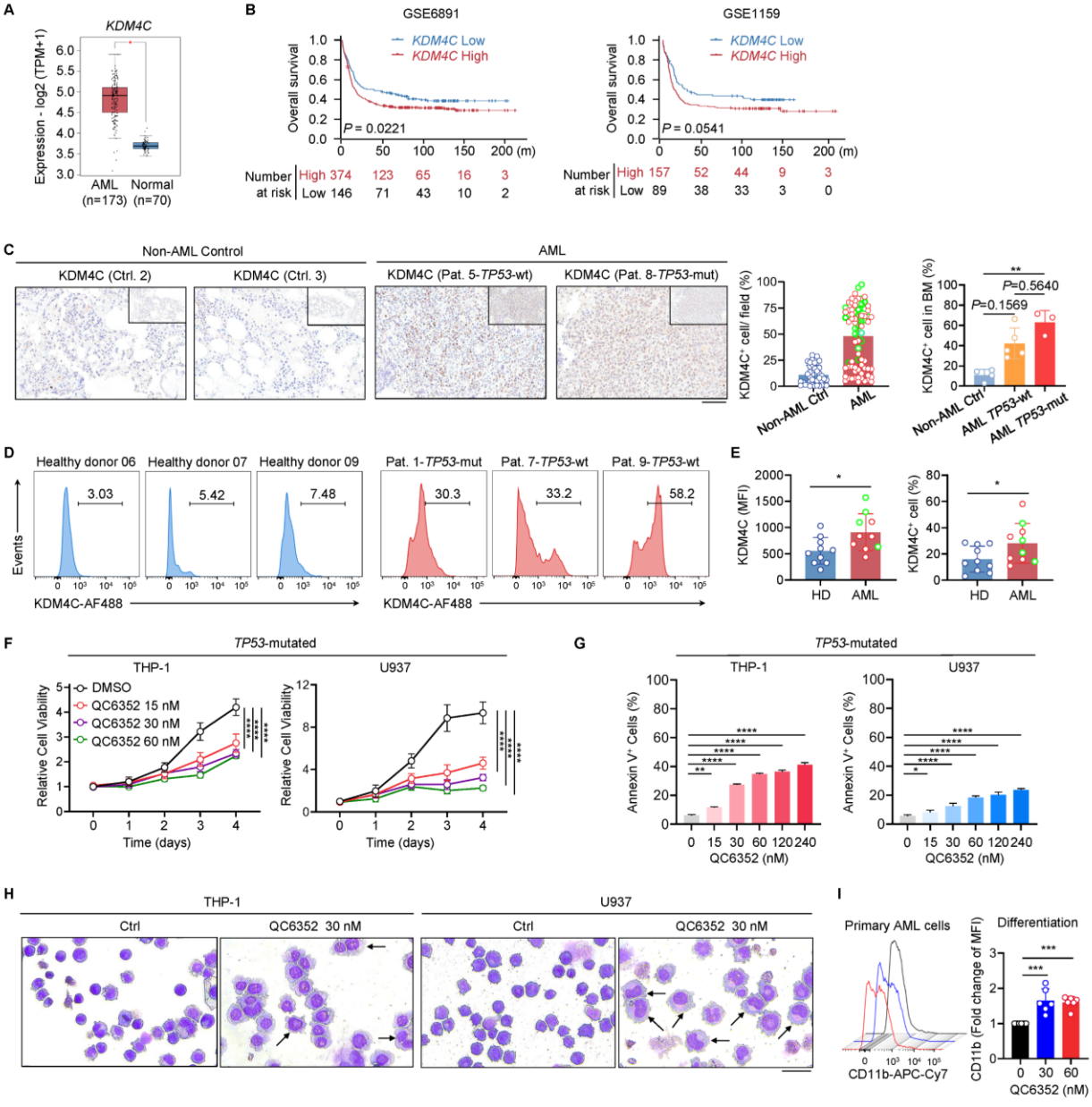

Figure 1. KDM4C is upregulated and associated with poor clinical outcomes in acute myeloid leukemia. (A) Box plot of the expression profile of *KDM4C* in AML samples (n = 173) and normal bone marrow samples (n = 70) from GEPIA. **(B)** Kaplan–Meier survival analysis of patients in the GSE6891 AML cohort (n = 520), stratified into low-*KDM4C*-expression (black, n = 146) and high-

KDM4C-expression (red, n = 374) groups, and patients in the GSE1159 AML cohort (n = 246), stratified into low-*KDM4C*-expression (black, n = 89) and high-*KDM4C*-expression (red, n = 157) groups. The optimal cutoff value was automatically selected separately for each cohort using the Kaplan–Meier Plotter database. *P* values were calculated using the log-rank (Mantel–Cox) test. n indicates the number of patients. **(C)** Representative immunohistochemical images showing KDM4C staining in bone marrow biopsy specimens from patients with AML and non-AML controls, together with field-level and patient-level quantification of the percentage of $KDM4C^+$ cells. Scale bars, 100 μm. The bar diagram (left) shows field-level quantification of the percentage of $KDM4C^+$ cells. Each dot represents one randomly selected microscopic field from specimens obtained from non-AML controls (n = 4) or patients with AML (n = 8), including three patients with *TP53*-mutated AML, shown in green. The bar diagram (right) shows patient-level quantification of the percentage of $KDM4C^+$ cells in bone marrow specimens from non-AML controls (n = 4) and patients with *TP53*-wild-type AML (n = 5) or *TP53*-mutated AML (n = 3). Each dot in the right graph represents one individual patient. **(D** and **E)** Flow cytometry plots (D) and corresponding quantification (E) of KDM4C mean fluorescence intensity (MFI; E, left) and the percentage of $KDM4C^+$ cells (E, right) among $CD33^+$ cells within total bone marrow mononuclear cells (BMMCs) isolated from healthy donors (n = 10) and patients with AML (n = 10). Data points from four patients with *TP53*-mutated AML are shown in green. **(F)** THP-1 and U937 cells were treated with the indicated concentrations of QC6352 for 1-4 days, and cell viability was assessed using the Cell Counting Kit-8 (CCK-8) assay (n = 6 biological replicates). **(G)** THP-1 and U937 cells were treated with the indicated concentrations of QC6352 for 48 h, and apoptosis was assessed by Annexin V/7-AAD staining and flow cytometry (n = 6 biological replicates). **(H)** Representative images showing the morphology of THP-1 and U937 cells treated with or without 30 nM QC6352, as assessed by Wright–Giemsa staining. Images are representative of at least three independent experiments. **(I)** Representative flow cytometry histogram (left) and bar diagram (right) showing the MFI of CD11b in primary *TP53*-mutated AML samples treated with vehicle, 30 nM QC6352 or 60 nM QC6352 for 48 h (n = 6 patients). The field-level data in panel C (left) are shown for descriptive purposes only, with each point representing one microscopic field; no inferential statistical analysis was performed at the field level. For the patient-level analysis in panel C (right), each point represents one independent patient. Patient-level data were analyzed using the Kruskal–Wallis test followed by Dunn's multiple-comparisons test, and adjusted *P* values are shown for all three pairwise comparisons; data in panel E were analyzed by two-tailed unpaired Student's *t* tests; data in panels F and G were analyzed by one-way ANOVA with Tukey's multiple comparisons test, and adjusted *P* values in panel F are shown for all six pairwise comparisons, and adjusted *P* values in panel G are shown for all 15 pairwise comparisons; data in panel I were analyzed by one-way repeated-measures ANOVA with Tukey's multiple comparisons test, and adjusted *P* values are shown for all three pairwise comparisons; $*P < 0.05$; $**P < 0.01$; $***P < 0.001$; $****P < 0.0001$. The data are presented as mean ± standard deviation.

QC6352 treatment also promoted the differentiation of *TP53*-mutated AML cells. Induction of differentiation contributes to the antileukemic effects of several therapeutic agents [23]. GSEA revealed that gene signatures associated with the positive regulation of myeloid leukocyte differentiation were enriched in QC6352-treated AML cells (Supplementary Fig. S1E). Wright–Giemsa staining further revealed morphological features consistent with myeloid differentiation following QC6352 treatment (Fig. 1H). Flow cytometric analysis also showed that QC6352 treatment markedly increased the expression of the myeloid differentiation markers CD11b and CD15 in *TP53*-mutated AML cells (Fig. 1I; Supplementary Fig. 1F-I).

QC6352 induced a senescence-associated phenotype in *TP53*-mutated AML cells.

Next, we investigated the mechanism by which QC6352 suppressed the proliferation of *TP53*-mutated AML cells *in vitro*. Flow cytometric analysis showed that QC6352-treated THP-1 and U937 cells exhibited significant increases in forward scatter (FSC) and side scatter (SSC), indicating increased cell size and intracellular complexity (Supplementary Fig. 3A). These changes were consistent with morphological features commonly associated with cellular senescence. In contrast, QC6352-treated *TP53*-wild-type AML cells exhibited a decrease in FSC accompanied by heterogeneous changes in SSC, a pattern consistent with apoptotic cell shrinkage and alterations in intracellular complexity (Supplementary Fig. 3B). We next evaluated whether QC6352 induced cellular senescence by examining multiple senescence-associated features, including senescence-associated β-galactosidase (SA-β-gal) activity, cell-cycle arrest, expression of cyclin-dependent kinase inhibitor genes, expression of senescence-associated secretory phenotype (SASP)-related inflammatory genes, reactive oxygen species (ROS) accumulation, and DNA damage. QC6352 treatment markedly increased SA-β-gal activity in primary *TP53*-mutated AML samples (Fig. 2A). Similarly, SA-β-gal activity was significantly increased in the *TP53*-mutated AML cell lines THP-1 and U937, whereas no comparable increase was observed in *TP53*-wild-type AML cell lines (Fig. 2B and C; Supplementary Fig. 3C). Cell-cycle analysis further showed that QC6352 treatment induced significant G0/G1-phase arrest in both THP-1 and U937 cells (Fig. 2D). Consistent with this finding, QC6352 treatment markedly increased the mRNA expression of *p21* and *p16* (Fig. 2E). Moreover, QC6352 increased the mRNA expression of SASP-associated inflammatory genes, including *IL8*, *IL6*, and *IL1B* (Fig. 2F).

Oxidative stress is an established inducer of cellular senescence and is also an important hallmark of the senescent phenotype, characterized by persistent ROS accumulation and mitochondrial dysfunction. GSEA revealed enrichment of oxidative stress- and senescence-

associated transcriptional programs in QC6352-treated THP-1 and U937 cells (Fig. 2G). Consistently, QC6352 treatment significantly increased mitochondrial and intracellular ROS levels (Fig. 2H-J). Because ROS accumulation can accompany cellular senescence and contribute to macromolecular damage, we next assessed γH2AX as a marker of DNA damage and examined cytosolic dsDNA accumulation. QC6352 treatment increased γH2AX levels and cytosolic dsDNA accumulation in *TP53*-mutated AML cells (Fig. 2K-M). These results indicate that QC6352 induces a senescence-associated phenotype in *TP53*-mutated AML cells, accompanied by ROS accumulation, DNA damage, and cytosolic DNA accumulation.

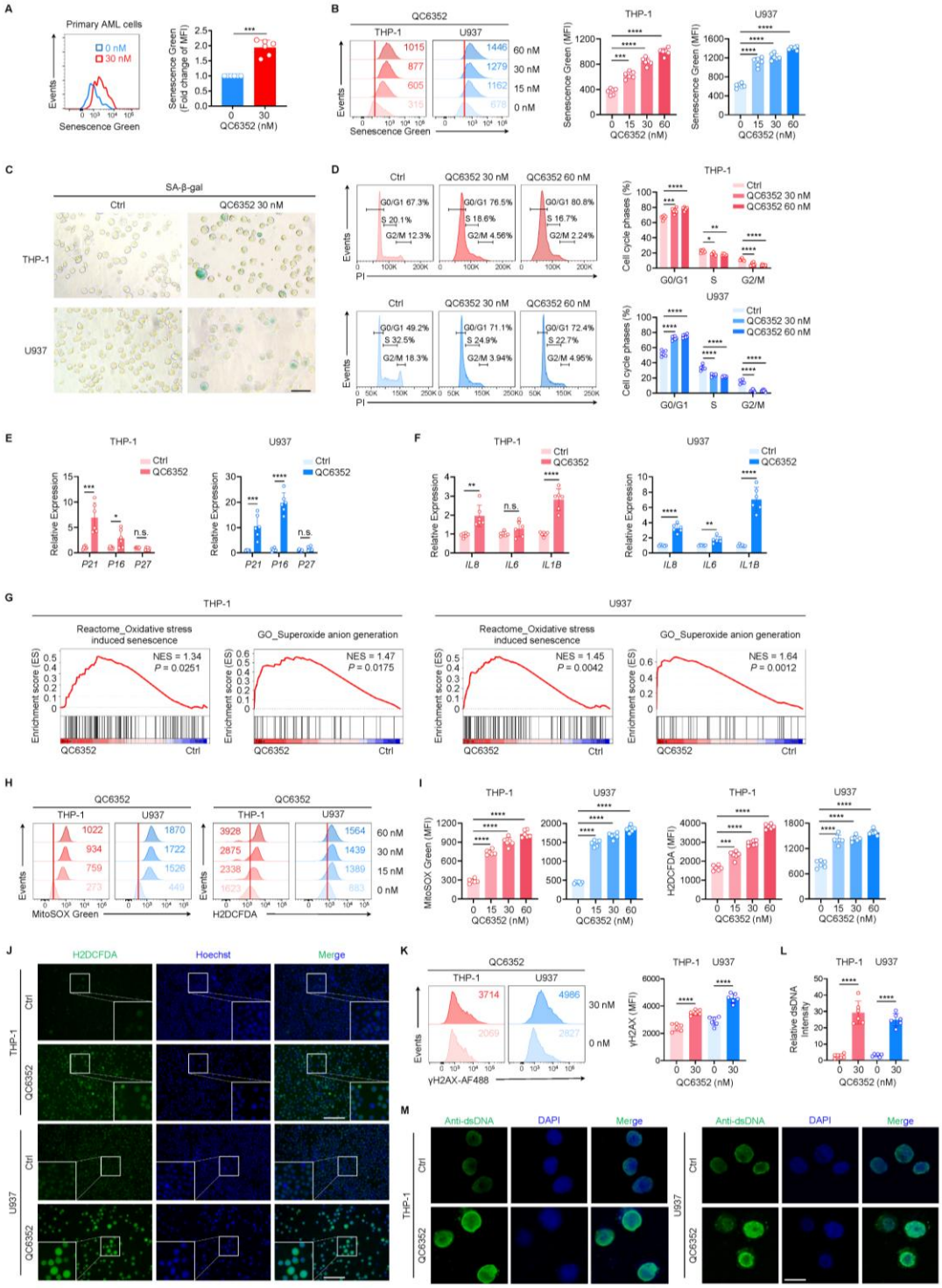

Figure 2. QC6352 induces a senescence-associated phenotype in *TP53*-mutated AML cells. **(A)** Representative flow cytometry histogram (left) and bar diagram (right) showing the fold change in MFI of senescence-associated β-galactosidase (SA-β-gal) in primary *TP53*-mutated AML samples treated with vehicle or 30 nM QC6352 for 48 h (n = 6 patients). **(B)** Representative flow cytometry histograms (left) and the bar diagrams (right) showing the MFI of SA-β-gal in THP-1 and U937 cells treated with the indicated concentrations of QC6352 for 48 h (n = 6 biological replicates). SA-β-gal was detected using Senescence Green fluorescent dye. **(C)** Representative micrographs showing SA-β-gal activity in THP-1 (top row) and U937 (bottom row) cells treated with vehicle or 30 nM QC6352 for 48 h. Scale bars, 50 μm. **(D)** Representative flow cytometry histograms and statistical analysis of cell-cycle distribution of THP-1 (top row) and U937 (bottom row) cells treated with the indicated concentrations of QC6352 for 48 h (n = 6 biological replicates). **(E)** RT-qPCR analysis of *P21*, *P16,* and *P27* mRNA expression in THP-1 and U937 cells treated with vehicle or 30 nM QC6352 for 48 h (n = 6 biological replicates). **(F)** RT-qPCR analysis of *IL8*, *IL6,* and *IL1B* mRNA expression in THP-1 and U937 cells treated with vehicle or 30 nM QC6352 for 48 h (n = 6 biological replicates). **(G)** GSEA plots of gene sets related to oxidative stress-induced senescence and superoxide anion generation in THP-1 (left) and U937 (right) cells treated with QC6352 or vehicle for 48 h. **(H and I)** Representative flow cytometry histograms (H) and bar diagrams (I) showing mitochondrial ROS and total cellular ROS levels in THP-1 and U937 cells treated with the indicated concentrations of QC6352 for 48 h (n = 6 biological replicates). Mitochondrial ROS was detected using MitoSOX Green fluorescent dye, and total cellular ROS was detected using H2DCFDA. **(J)** Representative fluorescence images showing total cellular ROS (green) and nuclei (blue) in THP-1 and U937 cells treated with vehicle or 30 nM QC6352 for 48 h. Scale bars, 100 μm. **(K)** Representative flow cytometry histograms and bar diagrams showing the MFI of γ-H2AX in THP-1 and U937 cells treated with vehicle or 30 nM QC6352 for 48 h (n = 6 biological replicates). **(L)** The bar diagram showing cytosolic dsDNA fluorescence intensity in THP-1 and U937 cells treated with vehicle or 30 nM QC6352 for 48 h. At least 50 cells per condition were randomly selected for analysis in each independent experiment, and the mean value obtained from the selected cells was treated as one biological replicate (n = 6 biological replicates). **(M)** Representative fluorescence images showing dsDNA (green) and nuclei (blue) in THP-1 and U937 cells treated with vehicle or 30 nM QC6352 for 48 h. Scale bars, 20 μm. Data in panel A were analyzed by two-tailed paired Student's t-test; data in panels E, F, K, and L were analyzed by two-tailed unpaired Student's *t* test; data in panels B and I were analyzed by one-way ANOVA with Tukey's multiple comparisons test, and adjusted *P* values are shown for all six pairwise comparisons; data in panel D were analyzed by one-way ANOVA with Tukey's multiple comparisons test, and adjusted *P* values are shown for all three pairwise comparisons; $*P < 0.05$; $**P < 0.01$; $***P < 0.001$; $****P < 0.0001$. The data are presented as mean ± standard deviation.

QC6352 increased NKG2D ligand expression in senescent *TP53*-mutated AML cells.

To further elucidate the effects of KDM4C inhibition in *TP53*-mutated AML, we performed transcriptomic profiling. RNA-sequencing analysis identified 827 and 915 significantly upregulated genes (log2 fold change > 1, adjusted *P* value < 0.05) in THP-1 and U937 cells, respectively, following QC6352 treatment. These genes included those encoding ligands for NK-cell-activating receptors (NK-ARs) and death receptors, as well as interferon-stimulated genes (Fig. 3A). Gene ontology (GO) enrichment analysis of the upregulated genes identified multiple immune-response-related biological processes in both cell lines following QC6352 treatment (Fig. 3B; Supplementary Fig. 4). Consistently, GSEA revealed significant enrichment of the NK-cell-mediated cytotoxicity pathway in QC6352-treated AML cells (Fig. 3C).

NK-cell activity is regulated by the dynamic balance between activating and inhibitory receptor signaling. Tumor cells can evade immune surveillance by downregulating ligands for NK-cell-activating receptors [24]. Transcriptomic analysis showed that QC6352 treatment upregulated NKG2D ligand genes, including *MICA*, *MICB*, and several members of the *ULBP* family, in *TP53*-mutated AML cells (Fig. 3D). These findings suggest that pharmacological targeting of KDM4C may enhance the immunogenicity of *TP53*-mutated AML cells. Flow cytometric analysis confirmed the corresponding increases in the cell-surface expression of NKG2D ligands at the protein level (Fig. 3E-H; Supplementary Fig. 5A-D). An increase in MICA/B expression was also observed in primary *TP*53-mutated AML samples following QC6352 treatment (Fig. 3I). In contrast, no comparable increase in NKG2D ligand expression was observed in the *TP53*-wild-type AML cell lines MOLM-13 and OCI-AML3 (Supplementary Fig. 5E). In addition, RNA-sequencing analysis revealed upregulation of *CALR*, and flow cytometric analysis showed increased cell-surface calreticulin (CRT) exposure following QC6352 treatment (Fig. 3D and J). Externalized calreticulin (ecto-CRT) serves as an immunogenic "eat-me" signal that can promote the recognition and phagocytic clearance of tumor cells by NK cells during immunogenic cell death [25].

To determine whether QC6352-induced changes in AML cells affected NK-cell activation, we co-cultured NK cells with THP-1 and U937 cells that had been pretreated with QC6352. NK cells co-cultured with QC6352-pretreated AML cells exhibited significantly increased expression of the activation marker CD69 and the activating receptors NKG2D, NKp30, and DNAM-1 (Supplementary Fig. 6A-D). These findings indicate that

QC6352 pretreatment of AML cells enhanced the activation phenotype of the co-cultured NK cells. The proportion of Ki-67$^+$ NK cells was also significantly increased following co-culture with QC6352-pretreated AML cells (Supplementary Fig. 6E). By contrast, no significant difference in the proportion of NKG2A$^+$ NK cells was observed between NK cells co-cultured with control and QC6352-pretreated AML cells (Supplementary Fig. 6F).

Together, these results indicate that pharmacological KDM4C inhibition with QC6352 increases NKG2D ligand expression in senescent *TP53*-mutated AML cells and is associated with enhanced activation of co-cultured NK cells.

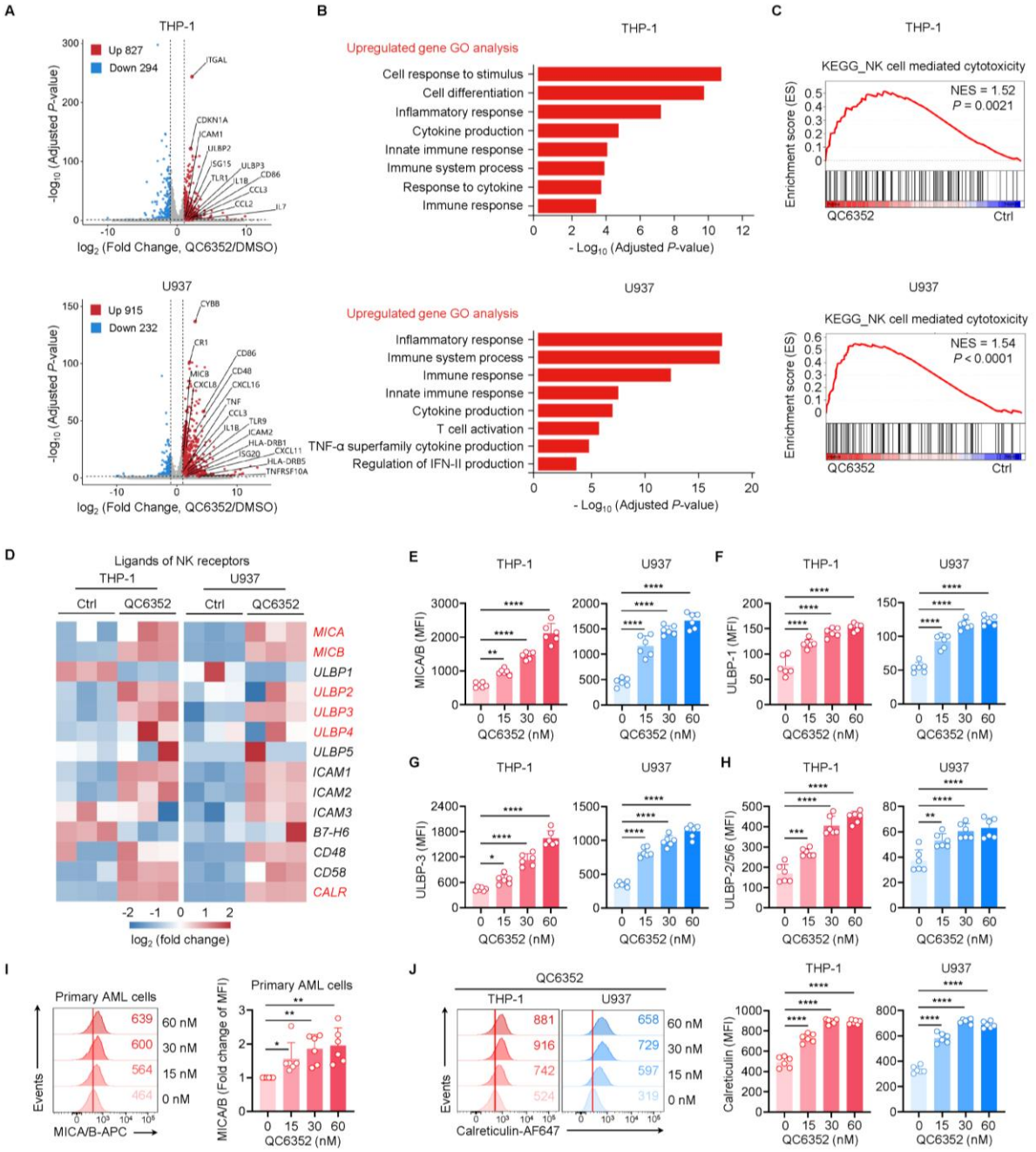

Figure 3. QC6352 upregulates NKG2D ligands and activates innate immune responses in *TP53*-mutated AML cells. (A) Volcano plots showing differentially expressed genes (DEGs: |log2 fold change| > 1 and adjusted *P* value < 0.05) in THP-1 and U937 cells treated with vehicle or 30 nM QC6352 for 48 h. **(B)** Bar diagrams showing the top eight biological processes enriched among the upregulated DEGs in THP-1 and U937 cells following QC6352 treatment for 48 h. **(C)** GSEA plots showing enrichment of the gene set associated with natural killer (NK) cell-mediated cytotoxicity in QC6352-treated THP-1 and U937 cells. **(D)** Heatmap showing the expression patterns of NK-cell ligand-related genes in THP-1 and U937 cells treated with vehicle

or 30 nM QC6352 for 48 h. **(E-H)** Bar diagrams showing the MFI of (E) MICA/B, (F) ULBP-1, (G) ULBP-3, and **(H)** ULBP-2/5/6 on THP-1 and U937 cells following treatment with the indicated concentrations of QC6352 for 48 h (n = 6 biological replicates). **(I)** Representative flow cytometry histograms (left) and bar diagram (right) showing the MFI of MICA/B on primary *TP53*-mutated AML cells treated with the indicated concentrations of QC6352 for 48 h (n = 6 patients). **(J)** Representative flow cytometry histograms (left) and bar diagram (right) showing the MFI of cell-surface calreticulin on THP-1 and U937 cells treated with the indicated concentrations of QC6352 for 48 h (n = 6 biological replicates). Data in panels E-H and J were analyzed by one-way ANOVA with Tukey's multiple comparisons test, and adjusted *P* values are shown for all six pairwise comparisons; data in panel I were analyzed by one-way repeated-measures ANOVA with Tukey's multiple comparisons test, and adjusted *P* values are shown for all six pairwise comparisons; $*P < 0.05$; $**P < 0.01$; $***P < 0.001$; $****P < 0.0001$. The data are presented as mean ± standard deviation.

QC6352 enhanced NK-cell-mediated antileukemic activity against *TP53*-mutated AML cells.

Next, we investigated whether pharmacologically targeting KDM4C in *TP53*-mutated AML cells using QC6352 could enhance NK-cell-mediated antileukemic activity. NK cells were isolated from human bone marrow mononuclear cells (BMMCs). Primary *TP53*-mutated AML cells and the *TP53*-mutated AML cell lines THP-1 and U937 were pretreated with vehicle, 30 nM QC6352, or 60 nM QC6352 and then washed before co-culture with NK cells. QC6352 pretreatment significantly increased NK-cell-mediated killing of primary AML cells (Fig. 4A). Similar results were observed in THP-1 and U937 cells, with QC6352 pretreatment enhancing NK-cell cytotoxicity across all effector-to-target (E: T) ratios tested (Fig. 4B-D).

Furthermore, the proportions of IFN-γ^+ TNF-α^+, IFN-γ^+ Granzyme B^+, and TNF-α^+ Granzyme B^+ polyfunctional NK-cell subsets, as well as the proportion of $CD107a^+$ NK cells, were significantly increased following co-culture with QC6352-pretreated AML cells (Fig. 4E-I). These findings indicate that pharmacological targeting of KDM4C with QC6352 increases the susceptibility of *TP53*-mutated AML cells to NK-cell-mediated killing and enhances NK-cell effector functions.

QC6352 enhanced NK-cell-mediated antileukemic activity partly through cGAS–STING signaling in *TP53*-mutated AML cells.

To further investigate the mechanisms underlying the effects of pharmacological targeting of KDM4C with QC6352 in *TP53*-mutated AML cells, we performed additional analyses of the RNA-seq data. GSEA revealed significant enrichment of transcriptional programs related to interferon (IFN) production and responses in QC6352-treated THP-1 and U937 cells (Fig. 5A and B). Multiple interferon-stimulated genes (ISGs) were also upregulated in QC6352-treated *TP53*-mutated AML cells (Fig. 5C). These findings were consistent with our earlier GO enrichment analysis, which identified enrichment of innate immune response-related biological processes following QC6352 treatment (Fig. 3B; Supplementary Fig. 4). RT-qPCR analysis further showed significantly increased transcript levels of *IFNA1*, *IFNB1*, and *CXCL10* in THP-1 and U937 cells following QC6352 treatment (Fig. 5D). Consistently, ELISA showed increased IFN-α secretion by *TP53*-mutated AML cells following QC6352 treatment (Fig. 5E and H).

The cGAS–STING pathway is a major cytosolic DNA-sensing pathway that promotes type I interferon production. STING activation and type I interferons can also enhance NK-cell effector functions, suggesting that this pathway may contribute to NK-cell responses in the tumor microenvironment [26, 27]. We therefore measured 2′3′-cGAMP, the second messenger produced following cGAS activation. QC6352 treatment for 48 h significantly increased 2′3′-cGAMP levels in both primary *TP53*-mutated AML blasts and *TP53*-mutated AML cell lines (Fig. 5F and G). No comparable increase was observed in *TP53*-wild-type AML cells (Supplementary Fig. 7). Together with the increased expression of type I interferon-related genes, these findings supported the activation of cGAS–STING signaling following QC6352 treatment.

To determine whether STING signaling contributed to the immune-related effects of QC6352, we treated AML cells with the STING inhibitor H-151. H-151 significantly attenuated the QC6352-induced upregulation of MICA/B and ULBPs on *TP53*-mutated AML cells (Fig. 5I; Supplementary Fig. 8A, C, and D). H-151 also partially reduced the QC6352-induced increase in IFN-α secretion. Conversely, treatment with the STING agonist di-ABZI increased IFN-α secretion by primary *TP53*-mutated AML cells (Fig. 5H).

We next investigated whether the enhancement of NK-cell-mediated antileukemic activity by QC6352 was partly dependent on STING signaling in AML cells. NK cells were co-cultured with AML cells treated with QC6352 alone or in combination with H-151. H-151 partially attenuated the QC6352-induced increase in NK-cell-mediated killing of *TP*53-mutated AML cells (Fig. 5J and K; Supplementary Fig. 8B). Compared with NK cells co-cultured with QC6352-pretreated AML cells, NK cells co-cultured with AML cells treated with QC6352 plus H-151 exhibited lower expression of NKG2D, NKp30, and DNAM-1, as well as a lower proportion of $CD69^+$ cells

(Fig. 5L and M; Supplementary Fig. 8E-H). Additional cytotoxicity and cytokine analyses further showed that H-151 partially reduced the QC6352-induced enhancement of NK-cell effector functions (Fig. 5N and O; Supplementary Fig. 8I). Conversely, activation of STING signaling in AML cells with di-ABZI enhanced NK-cell-mediated antileukemic activity (Fig. 5I-O; Supplementary Fig. 8A-I).

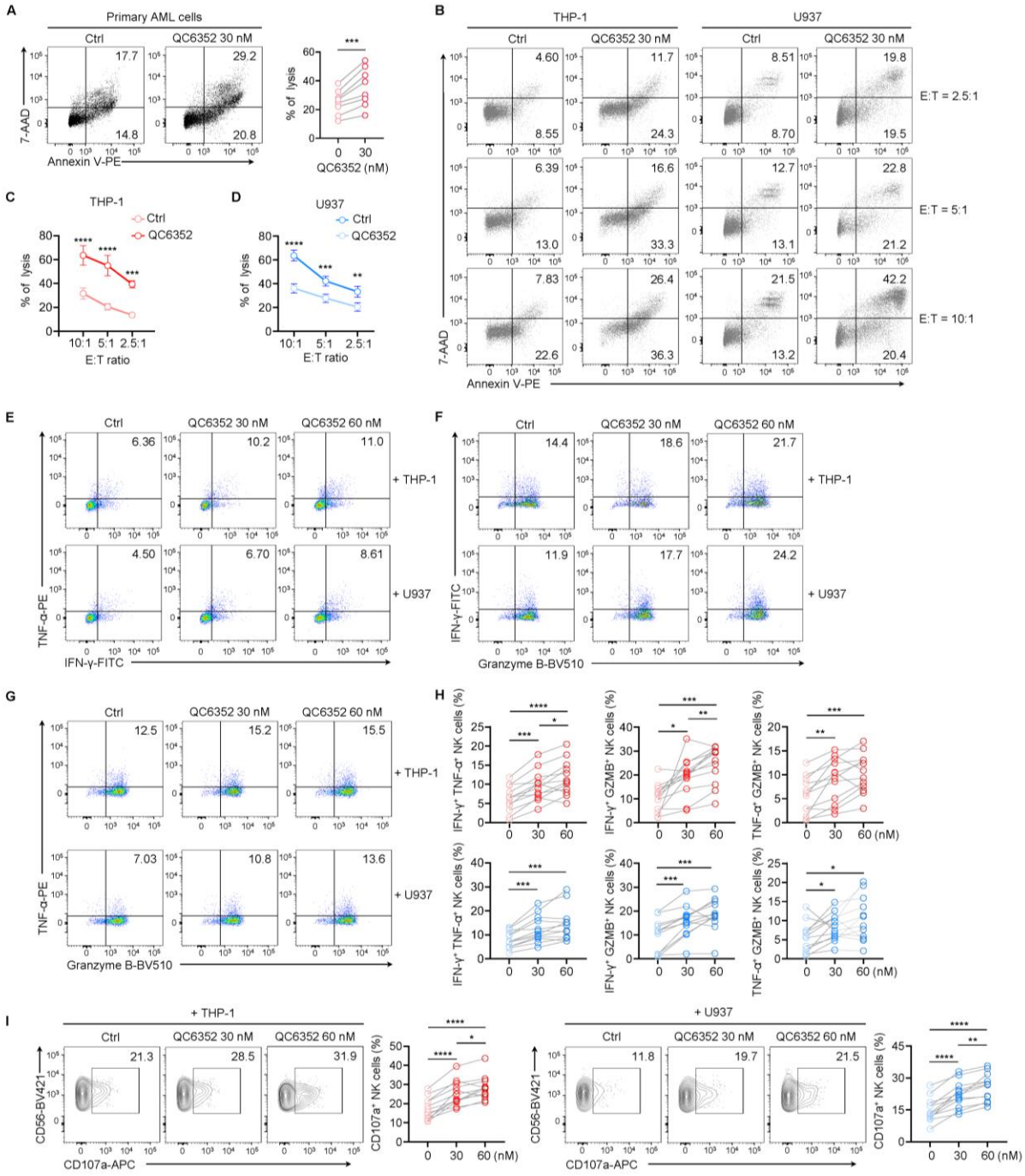

Figure 4. Targeting KDM4C in *TP53*-mutated AML cells with QC6352 enhances NK-cell-mediated antileukemic activity. **(A)** Flow cytometry plots and corresponding quantification showing the percentage of specific lysis of primary *TP53*-mutated AML cells by isolated bone marrow-derived NK (BMNK) cells. Primary AML cells were pretreated with vehicle or 30 nM QC6352 for 48 h, and then co-cultured with BMNK cells for 4 h. The effector-to-target (E: T) ratio was 5:1 (n = 8 patients). **(B)** Representative flow cytometry plots showing the percentage of specific lysis of THP-1 and U937 cells by BMNK cells. THP-1 and U937 cells were pretreated with vehicle or 30 nM QC6352 for 48 h and then co-cultured with BMNK cells for 4 h. The E: T ratio was titrated from 10:1 to 2.5:1 as indicated. One representative experiment from six independent experiments is shown. **(C** and **D)** Percentage of specific lysis of (C) THP-1 and (D) U937 cells by BMNK cells. THP-1 and U937 cells were pretreated with

vehicle or 30 nM QC6352 for 48 h and then co-cultured with BMNK cells for 4 h. The E: T ratio was titrated from 10:1 to 2.5:1 (n = 6 NK-cell donors). **(E-G)** Representative flow cytometry plots showing the proportions of (E) IFN-γ^+ TNF-α^+ NK cells, (F) IFN-γ^+ Granzyme B^+ NK cells, and (G) TNF-α^+ Granzyme B^+ NK cells among total BMNK cells after co-culture with THP-1 or U937 cells for 6 h. THP-1 and U937 cells were pretreated with vehicle or the indicated concentrations of QC6352 for 48 h, and the E: T ratio was 5:1. **(H)** Corresponding quantification of the proportions of IFN-γ^+ TNF-α^+ NK cells, IFN-γ^+ Granzyme B^+ NK cells, and TNF-α^+ Granzyme B^+ NK cells among total BMNK cells after co-culture with THP-1 or U937 cells for 6 h. THP-1 and U937 cells were pretreated with either vehicle or the indicated concentrations of QC6352 for 48 h, and the E: T ratio was 5:1 (n = 12 NK-cell donors). **(I)** Representative flow cytometry plots and corresponding quantification showing the proportion of $CD107a^+$ NK cells among total BMNK cells after co-culture with THP-1 or U937 cells for 6 h. THP-1 and U937 cells were pretreated with either vehicle or the indicated concentrations of QC6352 for 48 h, and the E: T ratio was 5:1 (n = 12 NK-cell donors). Data in panels A, C, and D were analyzed by two-tailed paired Student's *t* test; data in panels H and I were analyzed by one-way repeated-measures ANOVA with Tukey's multiple comparisons test, and adjusted *P* values are shown for all three pairwise comparisons; $*P < 0.05$; $**P < 0.01$; $***P < 0.001$; $****P < 0.0001$. The data are presented as mean ± standard deviation.

To examine whether QC6352-induced activation of the cGAS–STING pathway and upregulation of NKG2D ligands were associated with the senescence-associated response, we used Rapamycin to attenuate QC6352-induced senescence. Rapamycin substantially reduced QC6352-induced cGAS–STING signaling and MICA/B upregulation (Supplementary Fig. 9). These findings support the possibility that the senescence-associated phenotype contributes to the immune-related effects induced by QC6352.

Overall, our findings suggest that pharmacological targeting of KDM4C with QC6352 increases NKG2D ligand expression in senescent *TP53*-mutated AML cells and enhances NK-cell-mediated antileukemic activity, at least partly through cGAS–STING signaling in AML cells.

QC6352 enhanced NK-cell-mediated antileukemic activity *in vivo.*

Next, we evaluated the efficacy of QC6352 against *TP53*-mutated AML *in vivo*. A THP-1 xenograft model was established in NCG mice to assess the *in vivo* effects of QC6352 (Fig. 6A). QC6352 was well tolerated and significantly reduced the THP-1 leukemia burden (Fig. 6B; Supplementary Fig. 10A and B). *In vitro* experiments further showed that QC6352 had minimal effects on the viability of normal $CD34^+$ hematopoietic progenitor cells and immune cells, supporting its favorable safety profile (Supplementary Fig. 10C and D). To determine whether QC6352 enhanced the susceptibility of AML cells to NK-cell recognition *in vivo*, we examined MICA/B expression on THP-1 cells and the functional status of adoptively transferred human NK cells. Adoptively transferred human NK cells were detected in the bone marrow, spleen, and peripheral blood (Supplementary Fig. 11). Consistent with the *in vitro* findings, QC6352 induced cellular senescence and increased MICA/B expression in THP-1 cells *in vivo* (Fig. 6C and D; Supplementary Fig. 12A and B). In parallel, human NK cells recovered from mice receiving NK-cell infusion plus QC6352 exhibited increased activation, degranulation, and cytokine production compared with those recovered from mice receiving NK cells alone (Fig. 6E-G; Supplementary Fig. 12C-F). Consistently, the combination of QC6352 treatment and NK-cell infusion showed enhanced antileukemic activity, with the combination group exhibiting the lowest leukemia burden among all treatment groups.

The antileukemic effects of QC6352 were further evaluated in a second xenograft model established using U937-Luc cells (Fig. 6H). QC6352 treatment significantly reduced the leukemia burden and prolonged survival compared with vehicle treatment (Fig. 6I-K). Consistent with the findings from the THP-1 model, mice treated with QC6352 plus NK-cell infusion exhibited the slowest leukemia progression compared with vehicle-treated mice and mice receiving either QC6352 or NK cells alone (Fig. 6I-K). Moreover, pharmacological inhibition of STING with H-151 partially attenuated the enhanced antileukemic effect of QC6352 plus NK-cell infusion *in vivo* (Fig. 6I-K). These findings suggest that the enhancement of NK-cell-mediated antileukemic activity by QC6352 is at least partly dependent on STING signaling *in vivo*.

To better resemble clinical settings, we used human peripheral blood mononuclear cells (PBMCs) instead of purified NK cells for adoptive transfer into the xenograft model (Fig. 6L). Consistent with the findings from the NK-cell-reconstituted xenograft models, mice receiving PBMCs plus QC6352 exhibited significantly slower leukemia progression than those receiving PBMCs alone (Fig. 6M-O).

To assess the contribution of NK cells to the enhanced antileukemic effect of QC6352, NK cells were depleted from PBMCs using magnetic beads before adoptive transfer (Supplementary Fig. 12G). The enhanced antileukemic effect observed with QC6352 plus PBMC infusion was markedly attenuated after NK-cell depletion (Supplementary Fig. 12H and I). These findings indicate that NK cells make a substantial contribution to the improved antileukemic efficacy of QC6352 combined with PBMC infusion. Collectively, our *in vitro* and *in vivo* findings demonstrate that pharmacological inhibition of

KDM4C with QC6352 induces cellular senescence and increases NKG2D ligand expression in *TP53*-mutated AML cells, thereby enhancing antileukemic activity to which NK cells substantially contribute.

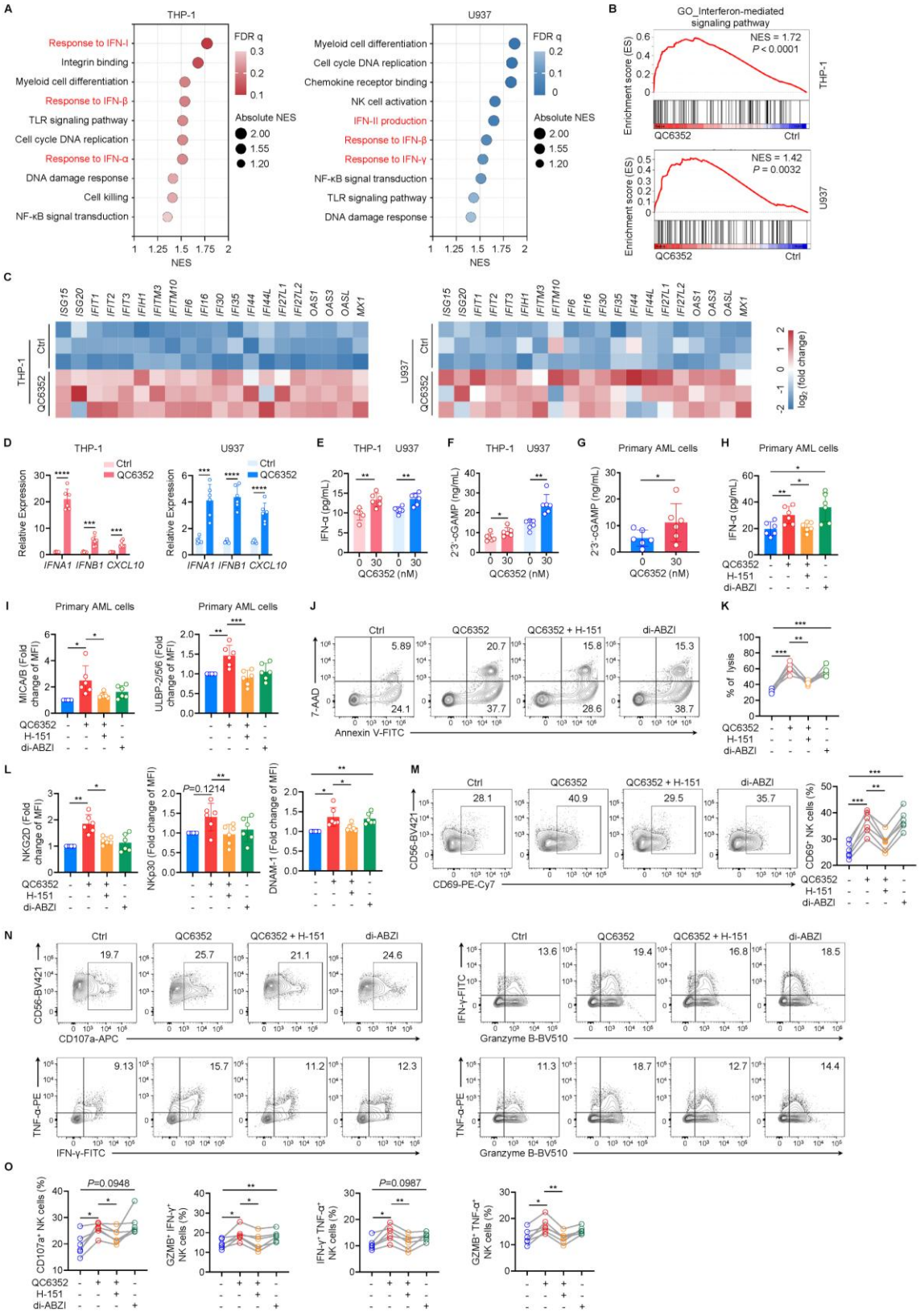

Figure 5. QC6352 enhances NK-cell-mediated antileukemic activity through activation of the cGAS–STING pathway in *TP53*-mutated AML cells. **(A)** Bubble plots showing the GSEA results from QC6352-treated THP-1 and U937 cells. **(B)** GSEA plots showing enrichment of the interferon-mediated signaling pathway gene set in THP-1 and U937 cells with treatment of QC6352. **(C)** Heatmap showing the expression patterns of interferon-stimulated genes (ISGs) in THP-1 and U937 cells treated with vehicle or 30 nM QC6352 for 48 h. **(D)** RT-qPCR analysis of *IFNA1*, *IFNB1,* and *CXCL10* mRNA expression in THP-1 and U937 cells treated with vehicle or 30 nM QC6352 for 48 h (n = 6 biological replicates). **(E)** ELISA measurement of IFN-α levels in the culture supernatants of THP-1 and U937 cells treated with vehicle or 30 nM QC6352 for 48 h (n = 6 biological replicates). **(F-G)** ELISA measurement of 2′3′-cGAMP levels in the culture supernatant of (F) THP-1 and U937 cells (n = 6 biological replicates) and (G) primary *TP53*-mutated AML cells (n = 6 patients) treated with vehicle or 30 nM QC6352 for 48 h. **(H)** ELISA measurement of IFN-α levels in the culture supernatants of primary *TP53*-mutated AML cells treated with vehicle, QC6352, QC6352 plus H-151, or di-ABZI for 48 h (n = 6 patients). **(I)** Bar diagrams showing the fold change in the MFI of MICA/B and ULBP-2/5/6 on primary *TP53*-mutated AML cells treated with vehicle, QC6352, QC6352 plus H-151, or di-ABZI for 48 h (n = 6 patients). **(J** and **K)** Representative flow cytometry plots (J) and corresponding quantification (K) showing the percentage of specific lysis of primary *TP53*-mutated AML cells by BMNK cells. Primary AML cells were pretreated with vehicle, QC6352, QC6352 plus H-151, or di-ABZI for 48 h, and then co-cultured with BMNK cells for 4 h. The E: T ratio was 5:1 (n = 6 patients). **(L)** Bar diagrams showing the fold change in the MFI of NKG2D, NKp30, and DNAM-1 on BMNK cells after co-culture with primary *TP53*-mutated AML cells for 48 h. Primary AML cells were pretreated with vehicle, QC6352, QC6352 plus H-151, or di-ABZI for 48 h. The E: T ratio was 5:1 (n = 6 patients). **(M)** Representative flow cytometry plots and corresponding quantification showing the proportion of $CD69^+$ NK cells among total BMNK cells after coculture with primary *TP53*-mutated AML cells for 24 h. Primary AML cells were pretreated with vehicle, QC6352, QC6352 plus H-151, or di-ABZI for 48 h. The E: T ratio was 5:1 (n = 6 patients). **(N** and **O)** Representative flow cytometry plots (N) and corresponding quantification (O) showing the proportions of $CD107a^+$ NK cells, IFN-γ^+ TNF-α^+ NK cells, IFN-γ^+ Granzyme B^+ NK cells, and TNF-α^+ Granzyme B^+ NK cells among total BMNK cells after co-culture with primary *TP53*-mutated AML cells for 6 h. Primary AML cells were pretreated with vehicle, QC6352, QC6352 plus H-151, or di-ABZI for 48 h. The E: T ratio was 5:1 (n = 6 patients). Data in panels D-F were analyzed by two-tailed unpaired Student's *t* test; data in panel G were analyzed by two-tailed paired Student's *t* test; data in panels H, I, K, L, M, and O were analyzed by one-way repeated-measures ANOVA with Tukey's multiple comparisons test, and adjusted *P* values are shown for all six pairwise comparisons; $*P < 0.05$; $**P < 0.01$; $***P < 0.001$; $****P < 0.0001$. The data are presented as mean ± standard deviation.

In addition, we used the Tumor Immune Estimation Resource (TIMER) to analyze the association between *KDM4C* expression in bulk tumor transcriptomic datasets and immune scores. *KDM4C* expression was negatively correlated with immune scores across several cancer types, including thyroid carcinoma, uterine corpus endometrial carcinoma and colon adenocarcinoma (Supplementary Fig. 13). These correlative findings are consistent with a potential association between lower *KDM4C* expression and a more immune-enriched tumor microenvironment.

DISCUSSION

TP53-mutated AML is one of the most aggressive subtypes of AML and is associated with an extremely poor prognosis. In this study, we demonstrated that KDM4C expression was elevated in AML and was correlated with unfavorable clinical outcomes. Interestingly, pharmacological inhibition of KDM4C with QC6352 induced distinct cellular responses in *TP53*-wild-type and *TP53*-mutated AML cells. In *TP53*-wild-type AML cells, QC6352 treatment predominantly induced apoptosis, whereas cellular senescence and the associated immunological changes were not observed. In contrast, QC6352 induced only limited apoptosis in *TP53*-mutated AML cells but strongly promoted cellular senescence. This senescence response was associated with marked suppression of cell proliferation, increased intracellular oxidative stress, and DNA damage, which may collectively contribute to activation of the cGAS–STING pathway. Activation of this pathway was accompanied by increased expression of NKG2D ligands on the surface of senescent *TP53*-mutated AML cells, thereby enhancing NK-cell-mediated antileukemic activity. Importantly, we further demonstrated that pharmacological inhibition of KDM4C in combination with NK-cell therapy prolonged survival *in vivo*.

Cellular senescence is a complex biological process characterized by tumor-suppressive features that can be therapeutically exploited for cancer treatment. In the present study, pharmacological inhibition of KDM4C induced proliferative arrest and cellular senescence specifically in *TP53*-mutated AML cells. Similar effects of KDM4C inhibition have also been reported in other myeloid neoplasms [28], melanoma [29], and gastric cancer harboring *TP53* mutations [22]. Cellular senescence can suppress tumor development by imposing stable growth arrest on malignant cells, with persistent cell-cycle arrest representing one of its defining hallmarks. We found that pharmacological inhibition of KDM4C induced G0/G1 cell-cycle arrest and upregulated the cyclin-dependent kinase inhibitors p21 and p16 in *TP53*-mutated AML cell lines. Other senescence-associated features were also observed following QC6352 treatment, including cellular enlargement, SA-β-gal

accumulation, development of a senescence-associated secretory phenotype, and DNA damage signaling. Notably, the accumulation of intracellular ROS may exacerbate DNA damage. A recent study in breast cancer demonstrated that genetic or pharmacological targeting of KDM4C induced severe oxidative stress by suppressing glutathione synthesis, thereby inhibiting tumor-cell proliferation [30]. Similarly, in *TP53*-mutated AML cells, QC6352 treatment induced the accumulation of both mitochondrial and total intracellular ROS. This ROS accumulation was accompanied by enhanced DNA damage signaling and cytosolic DNA accumulation, which may contribute to the establishment and maintenance of cellular senescence and proliferative arrest.

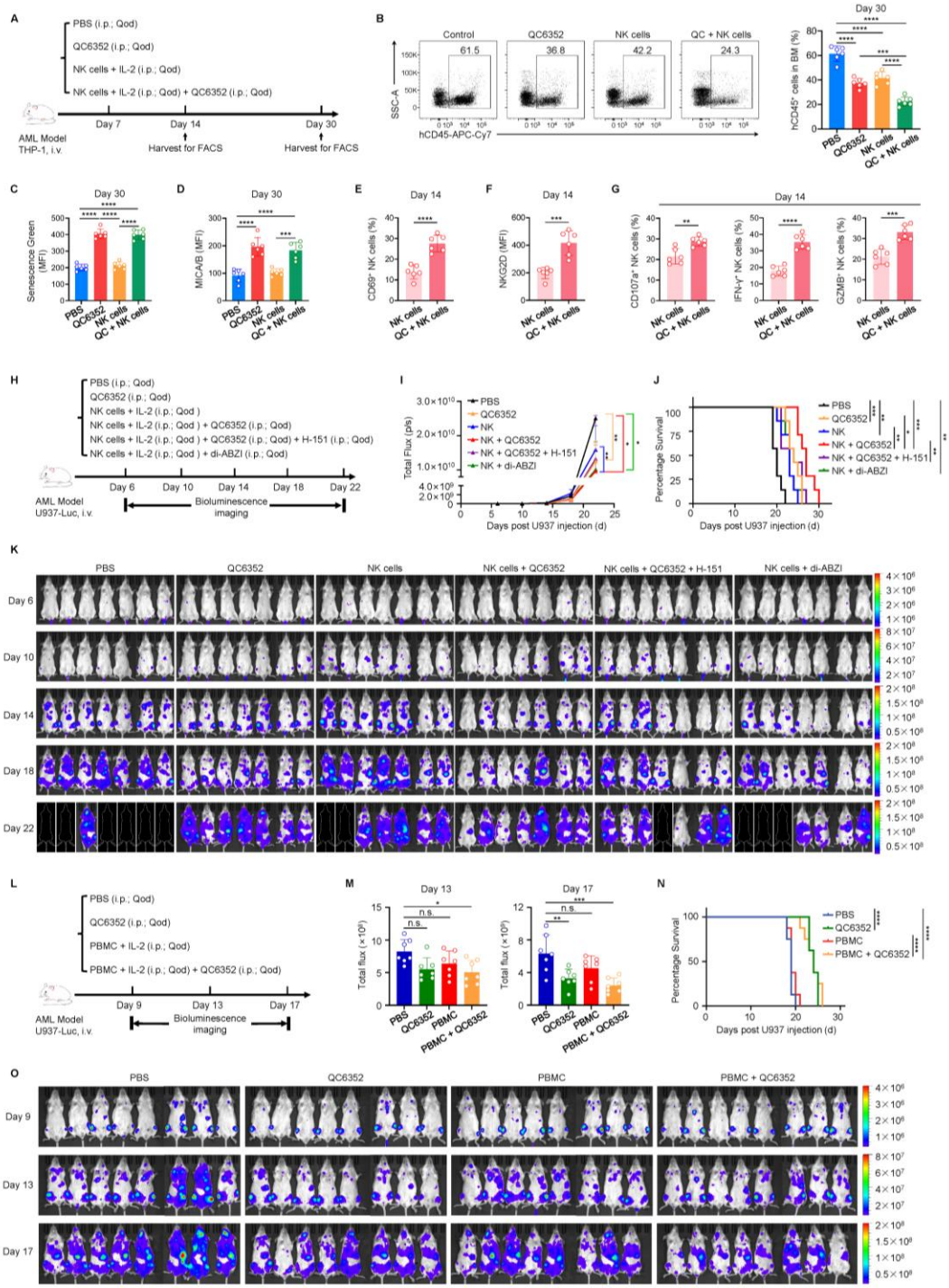

Figure 6. QC6352 enhances NK-cell-mediated antileukemic activity *in vivo*. (A) Experimental design: NCG mice were injected with 1×10^6 THP-1 cells via the tail vein. Seven days after THP-1 infusion, the mice were randomly assigned to four groups and treated with PBS (control), QC6352 (10 mg/kg, Qod), 5×10^6 NK cells, or 5×10^6 NK cells plus QC6352. On Day 14, six mice from each group were randomly euthanized. Bone marrow samples from the NK-cell and NK-cell-plus-QC6352 groups were collected for flow cytometric evaluation of the function of the adoptively transferred human NK cells. On Day 30, bone marrow samples were collected from the remaining six mice in each group to assess THP-1 cell engraftment by flow cytometry. **(B)** Representative flow cytometry plots and bar diagram showing the percentage of $hCD45^+$ cells in the bone marrow on Day 30 (n = 6 mice per group). **(C)** Bar diagram showing the MFI of SA-β-gal in THP-1 cells isolated from the bone marrow on Day 30 (n = 6 mice per group). SA-β-gal was detected by Senescence Green fluorescent dye. **(D)** Bar diagram showing the MFI of MICA/B on THP-1 cells isolated from the bone marrow on Day 30 (n = 6 mice per group). **(E)** Bar diagram showing the proportion of $CD69^+$ NK cells among total human NK cells in the bone marrow on Day 14 (n = 6 mice per group). **(F)** Bar diagram showing the MFI of NKG2D on human NK cells in the bone marrow on Day 14 (n = 6 mice per group). **(G)** Bar diagrams showing the proportions of $CD107a^+$, IFN-γ^+, and Granzyme B^+ NK cells among total human NK cells in the bone marrow on Day 14 (n = 6 mice per group). **(H)** Experimental design: NCG mice were injected with 1×10^5 luciferase-expressing U937 (U937-Luc) cells via the tail vein. After leukemic engraftment was confirmed by bioluminescence imaging (BLI) on Day 6, the mice were randomly assigned to six groups and treated with PBS (control), QC6352 (10 mg/kg, Qod), 5×10^5 NK cells, 5×10^5 NK cells plus QC6352, 5×10^5 NK cells plus QC6352 plus H-151 (15 mg/kg, Qod), or 5×10^5 NK cells plus di-ABZI (3 mg/kg, Qod). AML burden was monitored by BLI at the indicated time points. **(I)** Quantification of AML burden based on total flux (p/s) at the indicated time points (n = 7 mice per group). **(J)** Kaplan–Meier survival curves of mice bearing U937-Luc leukemia. Statistical significance was determined using the log-rank (Mantel–Cox) test (n = 7 mice per group). **(K)** Representative BLI images showing AML burden at the indicated time points. **(L)** Experimental design: NCG mice were injected with 1×10^5 U937-Luc cells via the tail vein. After leukemic engraftment was confirmed by BLI on Day 9, the mice were randomly assigned to four groups and treated with PBS (control), QC6352 (10 mg/kg, Qod), 1×10^6 PBMCs, or 1×10^6 PBMCs plus QC6352. AML burden was monitored by BLI at the indicated time points. **(M)** Quantification of AML burden based on total flux (p/s) at the indicated time points (n = 8 mice per group). **(N)** Kaplan–Meier survival curves of mice bearing U937-Luc leukemia. Statistical significance was determined using the log-rank (Mantel–Cox) test (n = 8 mice per group). **(O)** Representative BLI images showing AML burden at the indicated time points. Data in panels B-D and M were analyzed by one-way ANOVA with Tukey's multiple comparisons test, and adjusted *P* values are shown for all six pairwise comparisons; data in panel I were analyzed by one-way ANOVA with Tukey's multiple comparisons test, and adjusted *P* values are shown for all 15 pairwise comparisons; data in panels E-G were analyzed by two-tailed unpaired Student's *t* test; $*P < 0.05$; $**P < 0.01$; $***P < 0.001$; $****P < 0.0001$. The data are presented as mean ± standard deviation.

The tumor-suppressive effects of cellular senescence extend beyond the induction of stable proliferative arrest and can be further reinforced by extrinsic mechanisms, including enhanced immune surveillance and immunomodulation [31]. NK cells play a crucial role in the immune surveillance and clearance of senescent cells. Senescent tumor cells can recruit and activate NK cells by secreting inflammatory cytokines and chemokines, including CCL2, CXCL9, IL-12, and IL-15 [32]. In addition, senescent cells can upregulate ligands for activating receptors such as NKG2D and DNAM-1, as well as the IL-15/IL-15Rα complex and adhesion molecules such as ICAM-1, thereby promoting NK-cell-mediated recognition and elimination [33]. In our study, we found that the expression of MICA/B and ULBPs, which serve as key activating ligands for NKG2D, was significantly increased in *TP53*-mutated AML cells following pharmacological inhibition of KDM4C. Furthermore, human NK cells co-cultured with QC6352-pretreated AML cells exhibited enhanced activation and greater cytotoxic activity *in vitro* compared with those co-cultured with untreated AML cells. Consistent with these findings, adoptively transferred NK cells recovered from mice treated with QC6352 and infused with NK cells exhibited greater activation, degranulation, and cytokine production than those recovered from mice receiving NK-cell infusion alone. Previous studies have shown that *TP53* mutations in breast cancer cells can impair NK-cell activation and cytotoxicity [34, 35]. This impairment has been attributed to reduced expression of molecules involved in NK-cell recognition, including MICA/B, ULBPs, and ICAM-1, thereby limiting NK-cell-mediated recognition and elimination of tumor cells [36, 37]. Our findings demonstrated that pharmacological inhibition of KDM4C increased the expression of MICA/B and ULBPs on *TP53*-mutated AML cells, rendering these cells more susceptible to NK-cell-mediated killing. Collectively, these findings highlight the potential of pharmacological KDM4C inhibition as an adjunct strategy for NK-cell-based immunotherapy by enhancing the elimination of therapy-resistant *TP53*-mutated AML cells.

In recent years, activation of the cGAS–STING pathway has emerged as a crucial molecular link between cellular senescence and antitumor immunity [38-40]. In senescent cells, persistent DNA damage can promote the accumulation of cytosolic DNA, thereby activating the cGAS–STING pathway and inducing the production of type I interferons, inflammatory cytokines, and chemokines [41]. In the present study, pharmacological inhibition of KDM4C activated the cGAS–STING

pathway in *TP53*-mutated AML cells, as evidenced by increased cGAMP production and enhanced type I IFN responses. Robust type I IFN responses have been reported to activate multiple immune cell populations in the tumor microenvironment, particularly dendritic cells, T cells, and NK cells [11, 42, 43]. Furthermore, activation of the cGAS–STING signaling axis can inhibit tumor growth by directly inducing the expression of cell-surface ligands for NKG2D, including ULBPs [15]. Consistent with these observations, pharmacological inhibition of STING attenuated the QC6352-induced upregulation of MICA/B and ULBPs and reduced the cytotoxic activity of NK cells co-cultured with QC6352-pretreated AML cells. *In vivo*, STING inhibition partially attenuated the antileukemic effects of combined QC6352 treatment and NK-cell infusion, resulting in more rapid AML progression and shorter survival than those in mice receiving QC6352 plus NK-cell infusion.

However, cellular senescence has context-dependent effects on tumor progression. Although acute senescence can restrict malignant cell proliferation, the long-term persistence of senescent tumor cells and sustained secretion of senescence-associated factors may promote chronic inflammation, immunosuppression, and disease recurrence. Thus, the therapeutic benefit of senescence induction may depend on the efficient elimination of senescent cells by the immune system. In our study, pharmacological inhibition of KDM4C not only induced senescence-associated growth arrest in *TP53*-mutated AML cells but also enhanced their immunogenicity through activation of the cGAS–STING pathway and upregulation of NKG2D ligands. These changes enhanced NK-cell-mediated antileukemic activity, suggesting that KDM4C inhibition may couple tumor-cell senescence with immune surveillance. Therefore, rather than relying on senescence induction alone, combining pharmacological KDM4C inhibition with NK-cell-based immunotherapy may provide a more effective therapeutic strategy by simultaneously suppressing leukemic growth and promoting the clearance of senescent leukemic cells.

Limitations of the study

Several limitations of this study should be acknowledged. Although QC6352 has shown the highest reported biochemical potency against KDM4C and was used at concentrations intended to minimize broader inhibition of KDM4 family members, potential contributions from other KDM4 proteins or off-target effects cannot be completely excluded. Genetic depletion and rescue experiments using wild-type KDM4C or a catalytically inactive KDM4C mutant will therefore be required to further establish whether the observed senescence and immune-remodeling phenotypes are KDM4C-specific and dependent on its catalytic activity. In addition, the limited availability of viable and molecularly characterized primary specimens from patients with *TP53*-mutated AML precluded the establishment of a patient-derived xenograft model to further validate the efficacy of combined KDM4C inhibition and NK-cell therapy. Finally, the generalizability of these findings to other malignancies warrants further investigation.

Acknowledgements

We would like to thank Dr. Mengqing Gao (Department of Hematology, The First Affiliated Hospital of USTC, University of Science and Technology of China) for providing the U937-Luc cell line. We also thank all the residents and physicians in the Department of Hematology and Department of Laboratory Medicine who contributed to this study.

Authorship Contributions

Conceptualization, D.W., H.W., and H.L.; Methodology, D.W., X.Z., P.H., and M.G.; Formal analysis, D.W., X.Z., and P.H.; Resources, D.W., X.Z., Q.F., L.G., and H.Z.; Data curation, N.Z., X.Z., and K.J.; Writing – original draft, D.W., X.Z., and C.D.; Writing – review & editing, C.D. and H.W.; Visualization, D.W.; Supervision, H.W., H.L., and D.W.; Funding acquisition, D.W.

Funding

This work was supported by the National Natural Science Foundation of China (#82370217, #82500227), Anhui Provincial Department of Education Scientific Research Project (#2022AH030128), Anhui Provincial Natural Science Foundation (# 2308085Y46), the Open Project of Anhui Provincial Key Laboratory of Tumor Evolution and Intelligent Diagnosis and Treatment (#KFKT 202403), USTC Research Funds of the Double First-Class Initiative (#YD9110002019), and USTC Key Youth Innovation Fund (#WK9100000091).

Ethics approval and consent to participate

This research did not involve clinical experiments. All animal experiments were performed at the Institute of Health and Medicine, Hefei Comprehensive National Science Center. The animal experimental protocols were approved by the Ethics Committee of the Institute of Health and Medicine, Hefei Comprehensive National Science Center (approval No. IHM-AP-2025-007), and all procedures were conducted in accordance with the applicable national guidelines for the care and use of laboratory animals in China.

Competing interests

The authors declare that they have no competing interests.

Materials availability

This study did not generate any new unique reagents or materials.

Data and code availability

All data supporting the conclusions of this study are provided in the manuscript and its supplementary materials. The raw sequencing data generated in this study have been deposited in the Genome Sequence Archive for Human (GSA-Human) in the National Genomics Data Center under accession number HRA013401. The publicly available Gene Expression Omnibus (GEO) datasets GSE6891 and GSE1159 were used for survival analyses. This study did not generate any original code. Any additional information required to reanalyze the data reported in this work is available from the lead contact upon reasonable request.

Supplementary Materials

The Supplementary data can be found online at: www.aginganddisease.org/EN/10.14336/AD.2026.0432.

References

[1] Baliakas P, Soussi T (2025). The TP53 tumor suppressor gene: From molecular biology to clinical investigations. J Intern Med, 298:78-96.

[2] DiNardo CD, Erba HP, Freeman SD, Wei AH (2023). Acute myeloid leukaemia. Lancet, 401:2073-2086.

[3] Badar T, Nanaa A, Atallah E, Shallis RM, Craver EC, Li Z, et al. (2024). Prognostic impact of 'multi-hit' versus 'single-hit' TP53 alteration in patients with acute myeloid leukemia: results from the Consortium on Myeloid Malignancies and Neoplastic Diseases. Haematologica, 109:3533-3542.

[4] Daver NG, Iqbal S, Renard C, Chan RJ, Hasegawa K, Hu H, et al. (2023). Treatment outcomes for newly diagnosed, treatment-naïve TP53-mutated acute myeloid leukemia: a systematic review and meta-analysis. J Hematol Oncol, 16:19.

[5] Esteve J, Nagler A, Labopin M, Versluis J, Sanz J, Gedde-Dahl T, et al. (2025). Allogeneic Hematopoietic Cell Transplantation in Patients with Acute Myeloid Leukemia with Myelodysplasia-Related Genetic Features: Relevance of the Genetic Underlying Category. A Retrospective Analysis on Behalf of the Acute Leukemia Working Party of the EBMT. Am J Hematol, 100:954-962.

[6] Urrutia S, Wong TN, Link DC (2025). A clinical guide to TP53 mutations in myeloid neoplasms. Blood, 146:2157-2167.

[7] Nian Z, Dou Y, Shen Y, Liu J, Du X, Jiang Y, et al. (2024). Interleukin-34-orchestrated tumor-associated macrophage reprogramming is required for tumor immune escape driven by p53 inactivation. Immunity, 57:2344-2361.e2347.

[8] Ho N, Talvard-Balland N, Köhler N, Zeiser R (2025). Immune Escape of Acute Myeloid Leukemia after Transplantation. Blood Cancer Discov, 6:168-181.

[9] Wang D, Sun Z, Zhu X, Zheng X, Zhou Y, Lu Y, et al. (2022). GARP-mediated active TGF-β1 induces bone marrow NK cell dysfunction in AML patients with early relapse post-allo-HSCT. Blood, 140:2788-2804.

[10] Hansrivijit P, Gale RP, Barrett J, Ciurea SO (2019). Cellular therapy for acute myeloid Leukemia - Current status and future prospects. Blood Rev, 37:100578.

[11] Samson N, Ablasser A (2022). The cGAS-STING pathway and cancer. Nat Cancer, 3:1452-1463.

[12] Fahey CG, Cordova AF, Gedeon PC, Barbie DA (2026). Targeting STING to generate therapeutic anti-tumor immunity. Cancer Cell, 44:260-280.

[13] Zhang Z, Zhang C (2025). Regulation of cGAS-STING signalling and its diversity of cellular outcomes. Nat Rev Immunol, 25:425-444.

[14] Yan Y, Tan X, Song B, Yi M, Chu Q, Wu K (2025). Breaking barriers: the cGAS-STING pathway as a novel frontier in cancer immunotherapy. Cancer Commun (Lond).

[15] Timilsina S, Huang JY, Abdelfattah N, Medina D, Singh D, Abdulsahib S, et al. (2025). Epigenetic silencing of DNA sensing pathway by FOXM1 blocks stress ligand-dependent antitumor immunity and immune memory. Nat Commun, 16:3967.

[16] Zhao A, Zhou H, Yang J, Li M, Niu T (2023). Epigenetic regulation in hematopoiesis and its implications in the targeted therapy of hematologic malignancies. Signal Transduct Target Ther, 8:71.

[17] Wu Q, Young B, Wang Y, Davidoff AM, Rankovic Z, Yang J (2022). Recent Advances with KDM4 Inhibitors and Potential Applications. J Med Chem, 65:9564-9579.

[18] Jie X, Fong WP, Zhou R, Zhao Y, Zhao Y, Meng R, et al. (2021). USP9X-mediated KDM4C deubiquitination promotes lung cancer radioresistance by epigenetically inducing TGF-β2 transcription. Cell Death Differ, 28:2095-2111.

[19] Lang T, Xu J, Zhou L, Zhang Z, Ma X, Gu J, et al. (2021). Disruption of KDM4C-ALDH1A3 feed-forward loop inhibits stemness, tumorigenesis and chemoresistance of gastric cancer stem cells. Signal Transduct Target Ther, 6:336.

[20] Jie X, Chen Y, Zhao Y, Yang X, Xu Y, Wang J, et al. (2022). Targeting KDM4C enhances CD8(+) T cell mediated antitumor immunity by activating chemokine CXCL10 transcription in lung cancer. J Immunother Cancer, 10.

[21] Diepstraten ST, Yuan Y, La Marca JE, Young S, Chang C, Whelan L, et al. (2024). Putting the STING back into

BH3-mimetic drugs for TP53-mutant blood cancers. Cancer Cell, 42:850-868.e859.
[22] Wang K, Gong Z, Chen Y, Zhang M, Wang S, Yao S, et al. (2023). KDM4C-mediated senescence defense is a targetable vulnerability in gastric cancer harboring TP53 mutations. Clin Epigenetics, 15:163.
[23] Kovecses O, Mercier FE, McKeague M (2024). Nucleic acid therapeutics as differentiation agents for myeloid leukemias. Leukemia, 38:1441-1454.
[24] Wang D, Dou L, Sui L, Xue Y, Xu S (2024). Natural killer cells in cancer immunotherapy. MedComm (2020), 5:e626.
[25] Guilbaud E, Kroemer G, Galluzzi L (2023). Calreticulin exposure orchestrates innate immunosurveillance. Cancer Cell, 41:1014-1016.
[26] Tani T, Mathsyaraja H, Campisi M, Li ZH, Haratani K, Fahey CG, et al. (2024). TREX1 Inactivation Unleashes Cancer Cell STING-Interferon Signaling and Promotes Antitumor Immunity. Cancer Discov, 14:752-765.
[27] Kumar A, Taghi Khani A, Duault C, Aramburo S, Sanchez Ortiz A, Lee SJ, et al. (2023). Intrinsic suppression of type I interferon production underlies the therapeutic efficacy of IL-15-producing natural killer cells in B-cell acute lymphoblastic leukemia. J Immunother Cancer, 11.
[28] Ernst P, Schnöder TM, Huber N, Perner F, Jayavelu AK, Eifert T, et al. (2022). Histone demethylase KDM4C is a functional dependency in JAK2-mutated neoplasms. Leukemia, 36:1843-1849.
[29] Yu Y, Schleich K, Yue B, Ji S, Lohneis P, Kemper K, et al. (2018). Targeting the Senescence-Overriding Cooperative Activity of Structurally Unrelated H3K9 Demethylases in Melanoma. Cancer Cell, 33:322-336.e328.
[30] Li Z, Peluffo G, Stevens LE, Qiu X, Seehawer M, Tawawalla A, et al. (2025). KDM4C inhibition blocks tumor growth in basal breast cancer by promoting cathepsin L-mediated histone H3 cleavage. Nat Genet, 57:1463-1477.
[31] Wang L, Lankhorst L, Bernards R (2022). Exploiting senescence for the treatment of cancer. Nat Rev Cancer, 22:340-355.
[32] Dong Z, Luo Y, Yuan Z, Tian Y, Jin T, Xu F (2024). Cellular senescence and SASP in tumor progression and therapeutic opportunities. Mol Cancer, 23:181.
[33] Colucci M, Zumerle S, Bressan S, Gianfanti F, Troiani M, Valdata A, et al. (2024). Retinoic acid receptor activation reprograms senescence response and enhances anti-tumor activity of natural killer cells. Cancer Cell, 42:646-661.e649.
[34] Wu HH, Leng S, Eisenstat DD, Sergi C, Leng R (2025). Targeting p53 for immune modulation: Exploring its functions in tumor immunity and inflammation. Cancer Lett, 617:217614.
[35] Uddin MB, Roy KR, Hill RA, Roy SC, Gu X, Li L, et al. (2022). p53 missense mutant G242A subverts natural killer cells in sheltering mouse breast cancer cells against immune rejection. Exp Cell Res, 417:113210.
[36] Efe G, Rustgi AK, Prives C (2024). p53 at the crossroads of tumor immunity. Nat Cancer, 5:983-995.
[37] Belkahla S, Brualla JM, Fayd'herbe de Maudave A, Falvo P, Allende-Vega N, Constantinides M, et al. (2022). The metabolism of cells regulates their sensitivity to NK cells depending on p53 status. Sci Rep, 12:3234.
[38] Wang Q, Yu Y, Zhuang J, Liu R, Sun C (2025). Demystifying the cGAS-STING pathway: precision regulation in the tumor immune microenvironment. Mol Cancer, 24:178.
[39] De Cecco M, Ito T, Petrashen AP, Elias AE, Skvir NJ, Criscione SW, et al. (2019). L1 drives IFN in senescent cells and promotes age-associated inflammation. Nature, 566:73-78.
[40] Wu Y, Lu WM, Cui QR, Zhou J, Lu GD (2025). Metabolic Regulation of cGAS-STING Signaling in the Tumor Microenvironment: Dual Immune Roles and Therapeutic Implications. Cytokine Growth Factor Rev, 85:43-55.
[41] Hopfner KP, Hornung V (2020). Molecular mechanisms and cellular functions of cGAS-STING signalling. Nat Rev Mol Cell Biol, 21:501-521.
[42] Reen V, D'Ambrosio M, Søgaard PP, Tyson K, Leeke BJ, Clément I, et al. (2025). SMARCA4 regulates the NK-mediated killing of senescent cells. Sci Adv, 11:eadn2811.
[43] Tang Y, Tang S, Yang W, Zhang Z, Wang T, Wu Y, et al. (2024). MED12 loss activates endogenous retroelements to sensitise immunotherapy in pancreatic cancer. Gut, 73:1999-2011.